coatings

MDPI

Article

A Two-Dimensional Guidance Strategy to Fabricate Perovskite Gadolinium Aluminate Ceramic Film

Tao Zhang [1], Lu Chen [2], Jing Yao [2] and Qi Zhu [2,*]

[1] Shenyang National Laboratory for Materials Science, Northeastern University, 3-11 Wenhua Road, Shenyang 110819, China
[2] Key Laboratory for Anisotropy and Texture of Materials (Ministry of Education), School of Materials Science and Engineering, Northeastern University, Shenyang 110819, China
* Correspondence: zhuq@smm.neu.edu.cn; Tel.: +86-24-8367-2700

Abstract: Gadolinium aluminate is an effective host for doping with various ions, and it can emit various colors. However, it is not easy to prepare transparent ceramics of gadolinium aluminate using traditional methods, although transparent ceramics are very suitable for solid lighting. In this work, a two-dimensional guidance strategy has been successfully carried out for perovskite-structured aluminate ceramic film. Through the two-dimensional interfacial reaction, $GdAlO_3$:Eu^{3+} (GAP:Eu^{3+}) transparent ceramic films were successfully fabricated using nanosheets exfoliated from layered gadolinium hydroxide, a rare earth source. The final films were tested by characterization techniques, including XRD, SEM, TEM, FT-IR, PLE/PL spectroscopy, temperature-dependent PL spectroscopy, and luminescence decay analysis. The perovskite film of transparent ceramics can be obtained by calcining LRH nanosheets on the substrate of amorphous alumina at 1550 °C in air with a reaction time of 2 h. During the interface reaction, temperature-dependent element diffusion takes the dominant role, and increased reactants take in the reaction with increasing calcination temperature. The grain for ceramic film is only 2–5 μm, which is much smaller than that for bulk ceramic. This is mainly due to the lower temperature and the interface diffusion. Ceramic film has a high transmittance larger than 90% at the visible range. Upon UV excitation at 254 nm, the film exhibits intense emission at the red wavelength range. The outcomes described in this work may have wide implications for transparent ceramics and layered rare-earth hydroxides.

Keywords: transparent ceramics; gadolinium aluminate; ceramic film; layered rare-earth hydroxide

Citation: Zhang, T.; Chen, L.; Yao, J.; Zhu, Q. A Two-Dimensional Guidance Strategy to Fabricate Perovskite Gadolinium Aluminate Ceramic Film. *Coatings* **2022**, *12*, 1927. https://doi.org/10.3390/coatings12121927

Academic Editor: Alicia de Andrés

Received: 6 November 2022
Accepted: 2 December 2022
Published: 8 December 2022

1. Introduction

Recently, light-emitting diodes (LEDs) have attracted increased attention because of their high luminous efficiency, low energy costs and environmentally friendly nature [1,2]. Traditionally, LEDs were fabricated by combining an LED chip (such as InGaN) and phosphor powders. Taking the white LED as an example, the blue LED chip and the yellow garnet phosphor of $Y_3Al_5O_{12}$:Ce^{3+} (YAG:Ce^{3+}) are the two most important components. However, the glue used for the phosphor powders in LED chips is sensitive to high temperatures and varied humidity, so the mixture of glue and phosphor will age and peel off as time goes by [3–5]. Now, transparent ceramic is widely accepted as the preferred luminophore for LEDs because of its stability and high transparency [6]. Because transparent ceramics have high transmittance and can easily be prepared into bulk ceramics with various shapes, they are suitable for application in high-power and high-density devices, except for light-emitting devices [6]. Transparent ceramics can be used in optical components, scintillators, transparent armor, solid-state lasers, and solid-state lighting. Except for the transparent ceramics of garnet rare earth aluminates, such as $Y_3Al_5O_{12}$ and $Lu_3Al_5O_{12}$, perovskite rare-earth aluminate is another system for transparent ceramics [7–9]. The investigations of perovskite rare-earth aluminate mainly focus on the three systems of $GdAlO_3$, $LaAlO_3$ and $YAlO_3$, because in the 4*f* sublayer of Gd^{3+}, La^{3+}, and Y^{3+}, the electrons are half, fully, or not

filled [7,8]. Therefore, they are suitable hosts that can be doped with various activators and emit various emissions.

By comparison, there are a lot of investigations into $YAlO_3$ and $LaAlO_3$, while the studies on $GdAlO_3$ are rather limited. $GdAlO_3$ (GAP) has a tetrahedron unit cell structure with a = 5.305 Å, b = 7.448 Å, c = 5.254 Å, and the unit cell belongs to the orthogonal perovskite structure of ABO_3. However, $GdAlO_3$ is not a perfect perovskite; it is a distorted perovskite [9]. In the ideal perovskite, Gd^{3+} has various coordinations with oxygen atoms, changing from 12 to 8, while Al^{3+} only has one kind of 6 coordination with oxygen atoms. The structure has the space group of *Pbnm,* deviating from the cubic space group *Pm*3*m*, which is due to distortion from the octahedron of [BO_6]. The octahedral cluster of [AlO_6] is arranged along the *c* axis, and the polyhedron of [GdO_8] connects with the octahedron of [AlO_6] in a collinear or coplanar manner [9]. Because of its special crystal structure, it is possible to optimize or realize the varied luminescence through a modification of crystal structure and composition. Up to now, the doping ions employed for $GdAlO_3$ hosts are mainly Eu^{3+} (red) and Ce^{3+} (yellow), and a small number of other ions, including Yb^{3+} (yellow), Tb^{3+} (blue and green), Pr^{3+} (blue and red), Er^{3+} (green), $Er^{3+}/Yb^{3+}/Tm^{3+}$ (white), and Cr^{3+} and Mn^{4+} (near infrared) [10–18]. In addition, previous studies have focused on the optical properties of $GdAlO_3$ nanocrystals and phosphor powders, and the reports on $GdAlO_3$ transparent ceramics and ceramic films are rather limited.

More recently, we proposed a novel strategy to fabricate transparent ceramic film of garnet-structured $Y_3Al_5O_{12}$ (YAG) through an interface reaction using the exfoliated nanosheets of layered rare-earth hydroxides (LRHs) as the rare-earth source [6,19]. The outcomes pave a two-dimensional guidance strategy for transparent ceramic film, and they may have a demonstrative effect on other systems, including the perovskite system. LRHs can be exfoliated into nanosheets with single- or several-layer thickness, which are the building units for the fabrication of films with multifunctions owing to 2D morphologies [20]. It is not easy for larger rare earths to form LRHs, and Gd might be the boundary, so most layered rare-earth hydroxides are formed for the rare earths with smaller ionic radii, such as Eu, Tb, Sm, Ho, and Y [21]. However, most rare-earth aluminates are garnet-structured with the composition of $RE_3Al_5O_{12}$ for the smaller rare earths, while they are perovskite-structured for the larger rare earths with the composition of $REAlO_3$ [22]. Therefore, layered rare-earth hydroxides with larger rare-earth ionic radii are the possible candidates to fabricate perovskite-structured rare-earth aluminates films. On this basis, layered gadolinium hydroxides are the best choice to fabricate perovskite-structured aluminates films, because gadolinium is almost the largest element for layered rare-earth hydroxides in the processing window.

In this work, a two-dimensional guidance strategy has been successfully carried out for perovskite-structured aluminate ceramic film. Through the interfacial reaction, $GdAlO_3:Eu^{3+}$ (GAP:Eu^{3+}) films of transparent ceramic were fabricated using the exfoliated layered gadolinium hydroxide nanosheets as the rare-earth source. The final films were tested by characterization techniques, including XRD, SEM, TEM, FT-IR, PLE/PL spectroscopy, temperature-dependent PL spectroscopy, and luminescence decay analysis. The transparent film exhibits intense emission at the red wavelength range. In the following section, the synthesis and properties of the ceramic films are investigated in detail.

2. Experimental Section

2.1. Materials and Synthesis

The raw materials are rare-earth oxides of Gd_2O_3 and Eu_2O_3 with 99.99% purity (Huizhou Ruier Rare-Chem. Hi-Tech. Co., Ltd., Huizhou, China), and are the rare-earth source. Ammonia hydroxide (NH_4OH, 25 wt %), nitric acid (HNO_3, 67 wt %), and anhydrous ethanol (C_2H_5OH, 99.7%) were purchased from Sinopharm Chemical Reagent Co., Ltd. (Shanghai, China) The aqueous solutions of rare-earth nitrates were made by dissolving the powder of rare-earth oxides in hot nitric acid.

Synthesis of LRH crystals and exfoliation of LRH nanosheets. First, 2 mmol rare-earth nitrate solution of $Gd(NO_3)_3$ and $Eu(NO_3)_2$ (Gd:Eu molar ratio of 95:5) was prepared by stirring the mixed solution at room temperature. After adding a proper NH_4OH, the colloidal suspension was adjusted with a pH value around 7. After that, the white mixed suspension was moved to a 100 mL Teflon-lined autoclave. After the hydrothermal reaction, the products were collected through centrifugation. The LRH crystals were exfoliated into nanosheets by hydrothermal anion exchange followed by mechanical agitation in formamide, according to our previous work [20]. The dodecyl sulfate (DS^-, $C_{12}H_{25}OSO_3^-$)-intercalated LRH was obtained like the first preparation [23]. The products after ion exchange are called LRH-DS in the later text.

Film fabrication of GAP transparent ceramic. Exfoliated nanosheets were spin-coated on a substrate of amorphous alumina and then calcined at selected temperatures with the reaction time of 2 h. Through an interfacial reaction, films of $GdAlO_3$ (GAP) transparent ceramic were grown on the substrate.

2.2. Characterization

Phase identification was performed by X-ray diffractometry (XRD, Model Smart-Lab, Rigaku, Tokyo, Japan) under 40 kV/40 mA, using nickel-filtered Cu-Kα radiation (λ = 0.15406 nm). The scanning speed was 6.0°/2θ per minute and the scanning range was 5°–60°. The FT-IR spectra were performed by Fourier transform infrared spectroscopy (FT-IR, Model Nicolet iS5, Thermo Fisher Scientific, Madison, WI, USA) using the standard KBr method. The morphology and microstructure of the products were analyzed by field emission scanning electron microscopy (FE-SEM, Model JSM-7001F, JEOL, Tokyo, Japan) and transmission electron microscopy (TEM, Model JEM-2000FX, JEOL, Tokyo, Japan). A fluorescence spectrophotometer (Model FP-8600, JASCO, Tokyo, Japan) was used for luminescence analysis. It was equipped with a 150 W Xe-lamp and an integrating sphere (Model ISF-513, JASCO, Tokyo, Japan).

3. Results and Discussion

3.1. Synthesis of LRH Crystals and Exfoliation of Nanosheets

The XRD patterns of LRH are shown in Figure 1a. The synthesized product is layered rare-earth hydroxide, since the diffraction peaks match well to the reported diffraction data. The diffraction peaks of (002) and (004) confirm the unique layered structure, while the appearance of (220) confirms that the compounds have a well-developed layered structure [20,21]. It is interesting to find that the (00*l*) reflections shift strongly to the lower-angle side, whereas the (*hk*0) reflections remain at the same position after the anion exchange with DS^-. This phenomenon can be well understood by the layer distance increase in LRH-DS, which results in a significant change in the crystal plane perpendicular to the host layer without affecting other planes [24,25]. There are no other impurities, implying that the products have a single phase of LRH. Therefore, the incorporation of Eu^{3+} did not affect the XRD diffraction peaks of LRH (Figure 1a). Through the anion exchange with DS^-, the LRH-DS still remains the layered characteristic, but the layer distance becomes significantly larger than that for the original LRH (Figure 1a). Close observation of the small-angle XRD in Figure 1b shows that the 2θ value of LRH-DS shifts to the side of the smaller angle, so the interlayer distance increases from ~0.84 nm for the original LRH to ~2.61 nm for the ion-exchanged LRH-DS. Figure 1c shows FT-IR spectra for the original LRH and ion-exchanged LRH-DS, which further confirms the completed reaction of ion exchange. The absorption peak at a wavenumber larger than 3500 cm^{-1} indicates the existence of o hydroxyl (OH^-), and the absorption peaks at a wavenumber range larger than 3000 cm^{-1} but smaller than 3500 cm^{-1} indicate the existence of H_2O. At the same time, the shoulder peak at ~1634 cm^{-1} also indicates the existence of H_2O. The above results confirm that there is molecular water in the compounds. For the LRH sample, there is a sharp absorption peak at ~1389 cm^{-1}, which confirms the existence of free NO_3^- [26–28]. However, the vibration of free NO_3^- disappears for ion-exchanged LRH-DS. Instead, new

absorption peaks at ~1050 cm^{-1}, ~1173 cm^{-1}, ~1466 cm^{-1}, ~2845 cm^{-1}, ~2915 cm^{-1}, and ~2962 cm^{-1} are found through anion-exchange processing, which are assigned to the vibrations of OSO_3^-, -CH_2, and -CH_3, respectively, indicating that $C_{12}H_{25}SO_4^-$ (DS^-) has replaced the NO_3^- of LRH via anion exchange [26,27]. The FE-SEM images of LRH are shown in Figure 2a. The products are platelets with a lateral size of 1–2 μm, and the surface is smooth. However, they are irregular platelets rather than hexagon platelets, which are usually observed for LRHs [20,21]. After anion exchange, the thickness of LRH crystals significantly increases, and the interlayers are found to be obviously loose for the LEH-DS sample (Figure 2b). Dispersing the LRH-DS in formamide yielded the transparent suspension containing exfoliated nanosheets (Figure 2c,d). Under laser beam irradiation, the suspension exhibited a clear observable Tyndall effect (Figure 2e). The TEM observation finds that the exfoliated nanosheets are rather thin, but the surface is not smooth, with flocculent molecules on the nanosheets, which may be the residual DS^-. The nanosheets exfoliated from LRH are the important reaction source of rare earth for the fabrication of ceramic films.

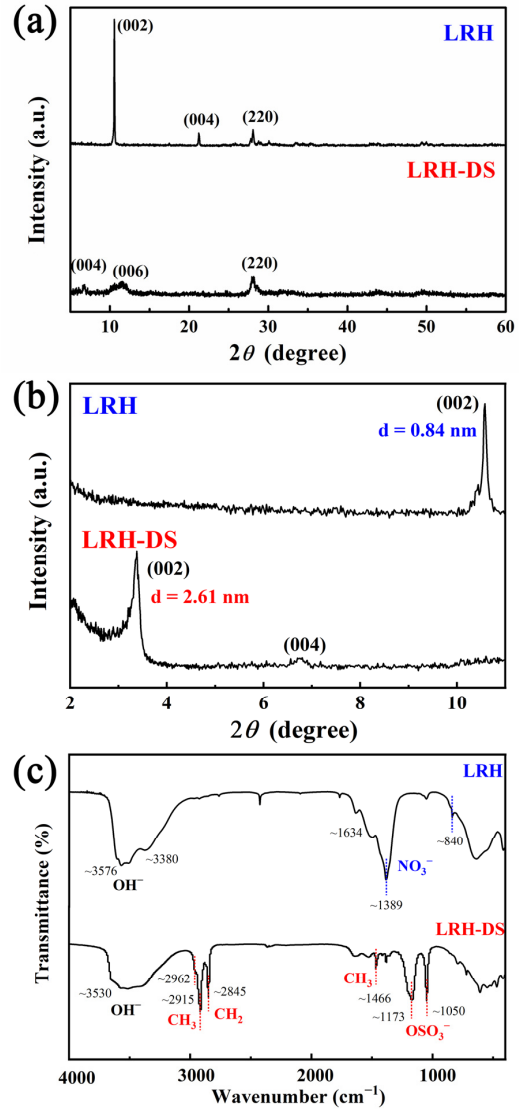

Figure 1. (**a**,**b**) XRD patterns and (**c**) FT-IR spectra for layered rare-earth hydroxide (LRH) and anion-exchanged product LRH-DS.

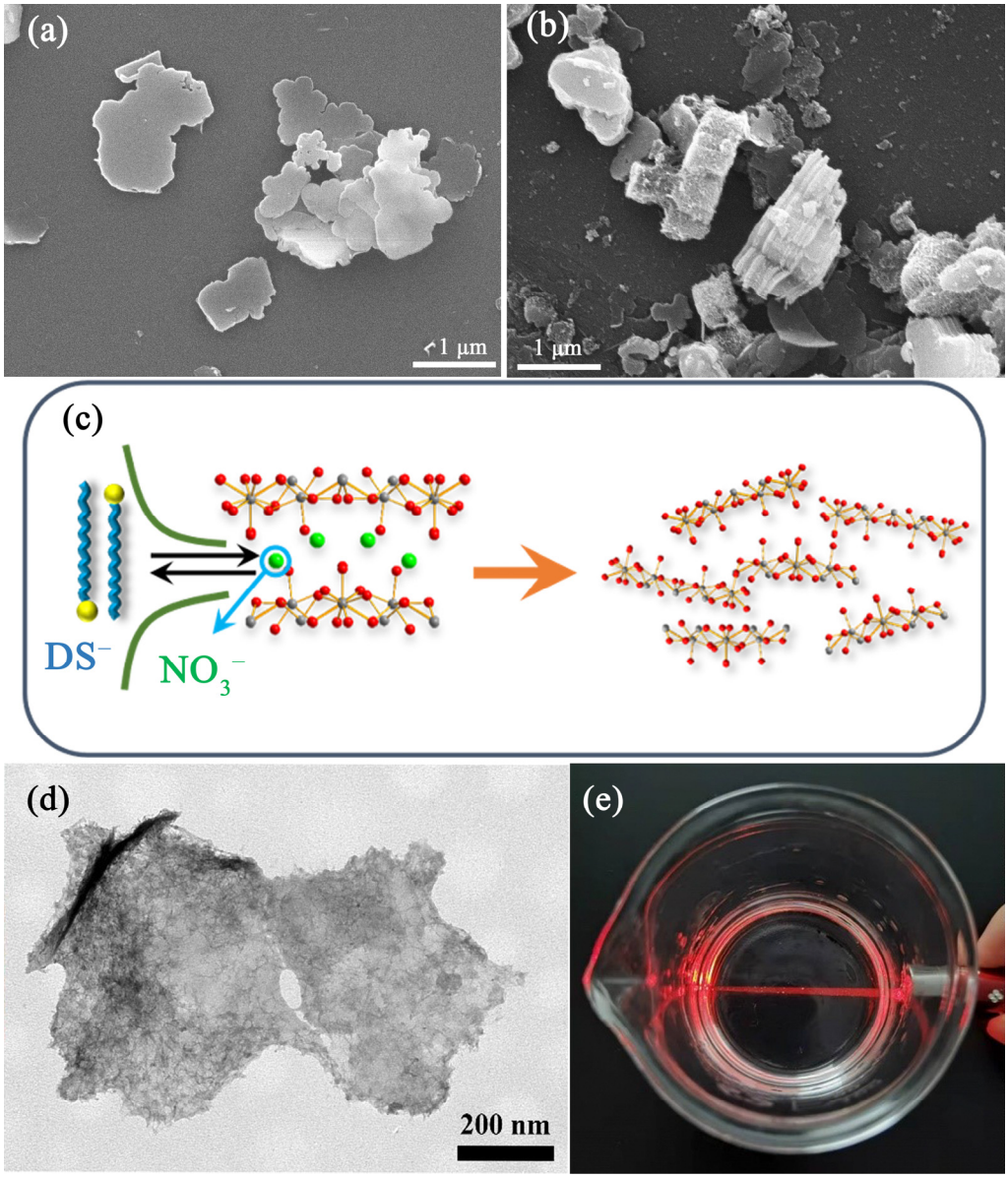

Figure 2. FE-SEM images of (**a**) layered rare-earth hydroxide and (**b**) anion-exchanged product. (**c**) Schematic illustration for nanosheet exfoliation. (**d**,**e**) TEM image of exfoliated nanosheets and colloidal suspension containing the exfoliated nanosheets.

3.2. Preparation and Characterization of GAP Ceramic Film

Figure 3 shows the schematic illustration for fabricating ceramic film of GAP and the formation mechanism. The exfoliated LRH nanosheets were directly prepared on the substrate of Al_2O_3 and calcined at selected temperatures for 120 min. The XRD patterns of prepared films at different temperatures are shown in Figure 4. After calcination at 800 °C, only cubic-structured Gd_2O_3 is found, which is converted from the exfoliated LRH nanosheets on Al_2O_3 substrate (Figure 4). Elevating the temperature from 800 °C to 1000 °C yields a small trace of $Gd_4Al_2O_9$ (GAM) along with the main Gd_2O_3, indicating that Al_2O_3 begins to react with Gd_2O_3 at the interface. When the temperature reaches 1300 °C, the main phase for the ceramic film is $GdAlO_3$, along with a small amount of $Gd_3Al_5O_{12}$ (GAG), $Gd_4Al_2O_9$ and crystalline Al_2O_3. Further increasing the temperature up to 1550 °C finally yields $GdAlO_3$ (GAP). The above results indicate that GAP is formed at a temperature higher than 1300 °C. Because the LRH nanosheets react with the amorphous alumina substrate at the interface, the temperature-dependent element diffusion takes the

dominant role, and more reactants participate in the reaction with increasing calcination temperature. At the low temperature of 800 °C, the LRH transforms into Gd_2O_3 and Al_2O_3 does not react with Gd_2O_3, because element diffusion does not happen. However, at a temperature of 1000 °C, some element diffusion takes place from Gd_2O_3 and Al_2O_3, which leads to the appearance of a small amount of $Gd_4Al_2O_9$ along with the main-phase Gd_2O_3. The element diffusion becomes stronger at the higher temperature of 1300 °C, and the reaction between Gd_2O_3, Al_2O_3, and $Gd_4Al_2O_9$ is more thorough, which finally contributes to the main $GdAlO_3$ and a small amount of $Gd_3Al_5O_{12}$ and $Gd_4Al_2O_9$. Because the thicknesses of the films are not uniform, the amount of Gd_2O_3 that participates in the reaction is not the same, and the resultant phases are not the same at different areas of the ceramic film. However, the almost uniform film that makes the dominant phase is $GdAlO_3$. At a temperature of 1300 °C, the crystallization of the amorphous alumina takes place, so some crystalline Al_2O_3 appears in the films. However, the Al_2O_3 for the interface reaction is completely in excess (Figure S1), so all the Gd_2O_3 reacts with Al_2O_3 to form $GdAlO_3$ at a temperature of 1550 °C. All crystalline Al_2O_3 at the interface participates in the reaction, so there is no crystalline Al_2O_3 in the film or a small trace of crystalline Al_2O_3 under the film that is undetectable.

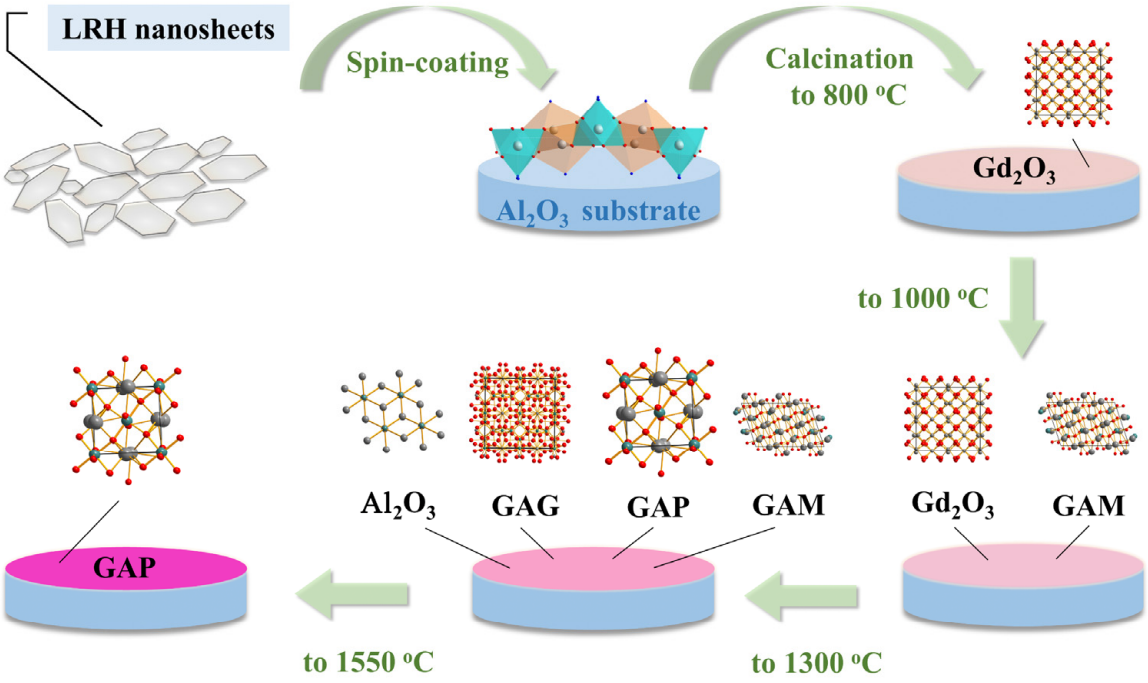

Figure 3. Schematic illustration for the fabrication of $GdAlO_3$ (GAP) ceramic films using exfoliated nanosheets as the rare-earth source. The intermediates GAM and GAG represent $Gd_4Al_2O_9$ and $Gd_3Al_5O_{12}$, respectively.

The SEM morphology of the films calcined at 1300 and 1550 °C is shown in Figure 5a,b. Traditionally, the obtained grain size of bulk ceramic is around 10–30 μm, because the ceramic is prepared by the traditional method at a high temperature range from 1700 °C to 1800 °C with the help of vacuum sintering [29–31]. Here, the sizes of most grains for the ceramic film at 1300 °C are 0.3–1 μm (Figure 5a). The grain size is up to 2–5 μm with the temperature elevated up to 1550 °C (Figure 5b). However, the grains are much smaller than those in bulk ceramic. First, the reaction temperature for ceramic film (1550 °C in air) is lower than that for bulk ceramic. Second, the reaction takes place on the interface, so the element diffusion is interface diffusion, which is rather slower than the volume diffusion for bulk ceramic. Therefore, the growth speed of the grains is much smaller than that for bulk ceramic.

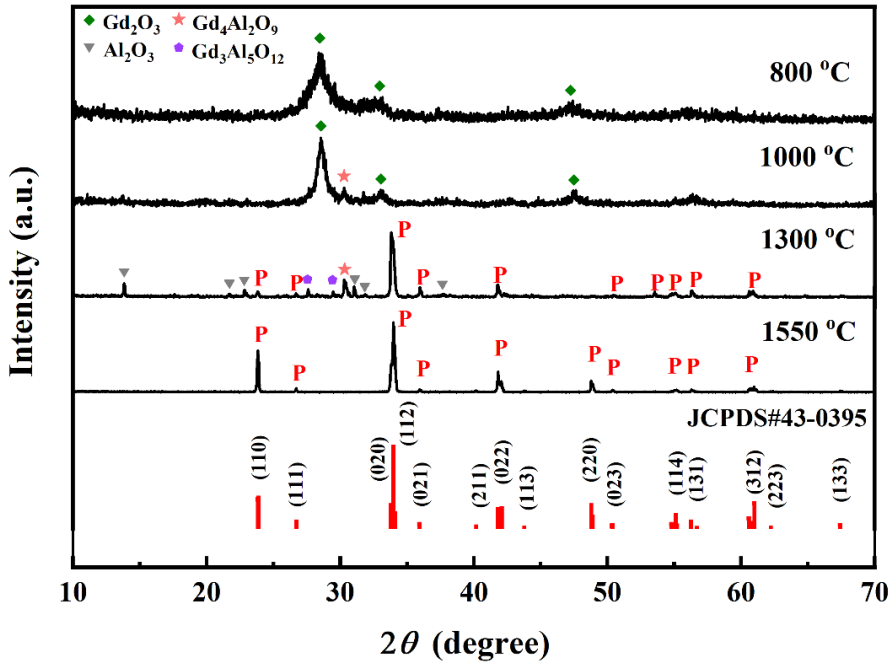

Figure 4. XRD patterns of the ceramic film calcined at different temperatures.

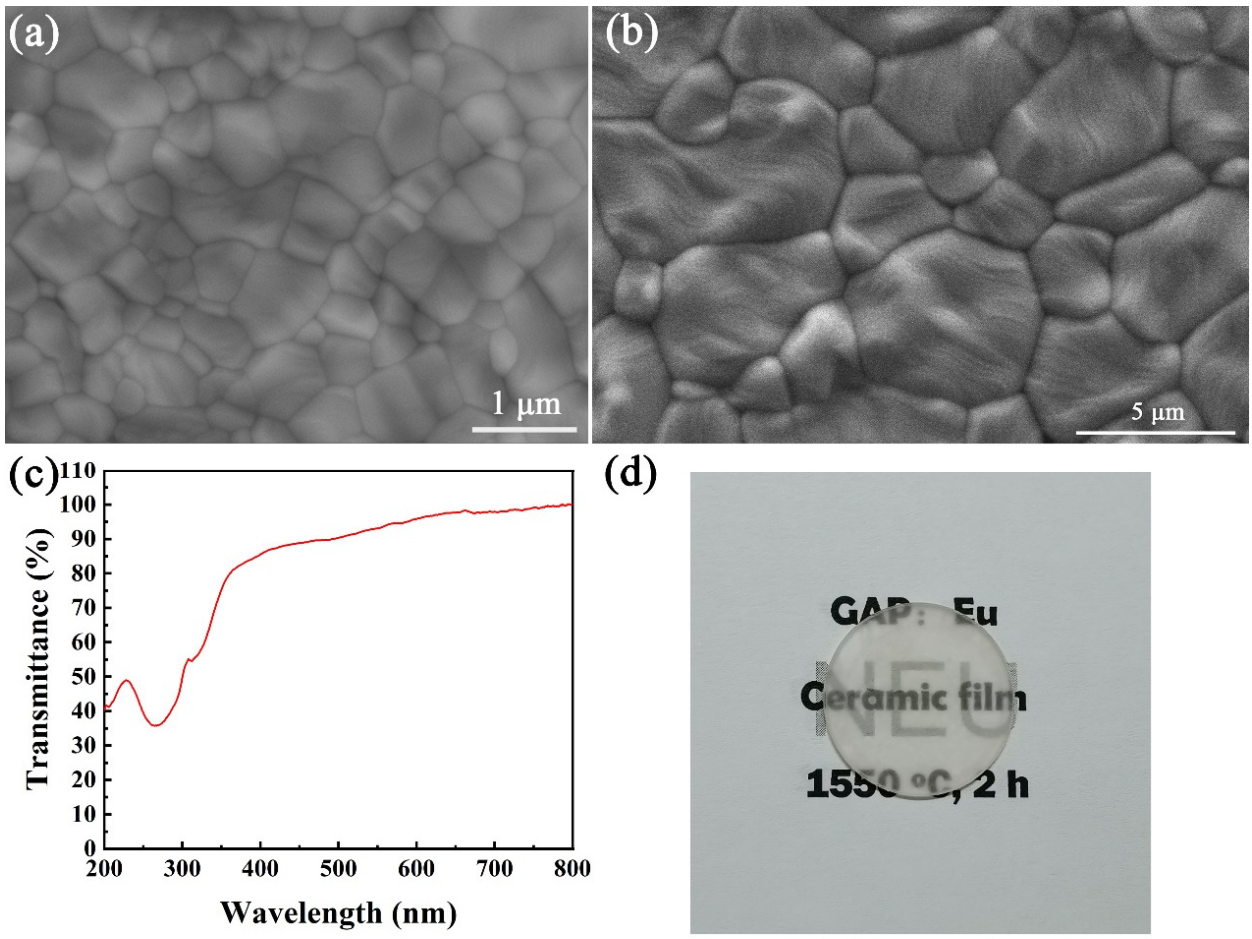

Figure 5. (**a**,**b**) FE-SEM images of the ceramic film calcined at 1300 °C and 1550 °C. (**c**) Transmittance curve and (**d**) appearance of the ceramic film calcined at 1550 °C.

3.3. Optical Properties of GAP:Eu^{3+} Transparent Ceramic Film

Transmittance of the prepared GAP:Eu^{3+} ceramic film was analyzed in Figure 5c. A broad and strong band is found in the transmittance curve at the range of 250–400 nm, which is arising from the charge-transfer absorption of O^{2-}-Eu^{3+} [32]. The shoulder near the intense band is assigned to the $^8S_{7/2}$-^6I_J transition of Gd^{3+} [33]. However, the transmittance curve is gentle and the value keeps above 90%, indicating that the transmittance of ceramic film is higher than 90%. Because the bare amorphous alumina substrate has a transmittance of ~99%, the ceramic film with the transmittance higher than 90% is highly transparent. Putting ceramic film (coated on the amorphous alumina) on the words shows that the words can also be observed clearly (Figure 5d), which confirms that GAP:Eu^{3+} ceramic film has high transmittance.

Figure 6 shows the photoluminescence excitation emission spectra of GAP:Eu^{3+} transparent ceramic film. Monitoring the wavelength at 618 nm, a broad and strong band is observed in PLE spectra at the range of 200–300 nm, whose maximum is located at 254 nm. The electron transition of O^{2-}-Eu^{3+} mainly contributes to the intense band (Figure 6a), which is usually called the charge-transfer band (CTB) [32]. However, the very weak peaks at the wavelength range of 300–500 nm are assigned to the intra-4f electronic transitions of the Eu^{3+} ion, but they are almost invisible because of the rather strong CTB. Under the UV light excitation at 254 nm, the GAP:Eu^{3+} transparent ceramic film outputs a red emission with multiple sharp peaks. The emission peaks at the range of 500–800 nm are assigned to the typical transition of Eu^{3+} from the excited energy level of $^5D_0$ to the ground energy level of ^7F_J (J = 0, 1, 2, 3, 4) [32]. Because the relative intensity of different J-level transitions is closely related to the symmetrical environment of Eu^{3+} ion, the coordination environment of Eu^{3+} in the host can be evaluated by the intensity of Eu^{3+} transitions. On the basis of the Judd–Ofelt theory, when the Eu^{3+} ion occupies a site with an inversion center, the magnetic dipole transition of $^5D_0$-$^7F_1$ is allowed, but the electric dipole transition of $^5D_0$-$^7F_2$ is forbidden [34,35]. In Figure 6b, the intensity of $^5D_0$-$^7F_1$ transition at 595 nm is obviously weaker than that of $^5D_0$-$^7F_2$ transition at 618 nm, so most Eu^{3+} ions occupy an asymmetry site. The symmetry of these sites is lower than that of the perfect crystal (D_{2d}), which leads to the appearance of $^5D_0$-$^7F_2$ transition at 618 nm and thus contributes to its emission intensity. Notably, the width of the peak around 617 nm indicates the overlap of bands corresponding to $^5D_0$-$^7F_2$ transitions (Figure 6b). Therefore, the outputted signal is red instead of orange. The CIE coordinate diagram of transparent ceramic film indicates that the color coordinate is (0.644, 0.355), located in the region of red color (Figure 6c). The CIE coordinate for the red emission of Eu^{3+} ions is close to the value in Ref. [13]. It not only depends upon the asymmetric ratio, but also on the higher energy emission levels. The appearance of the transparent ceramic film under UV light directly confirms the emission color is red. The transparent ceramic film also exhibits a stable thermality since its emission intensity only loses about 17% by increasing the environment temperature from 25 to 150 °C (Figure S2).

The lifetime of GAP:Eu^{3+} ceramic film is analyzed in Figure 6d through the fluorescence decay curve. The tested data are matched well with a single exponential, according to the following formula: $I = A\exp(-t/\tau)+B$, where τ is fluorescence lifetime (ms), t is decay time (ms), I is fluorescence intensity, and A and B are constants [19,36,37]. Through the calculation from the formula, the fluorescence lifetime of the film is determined to be ~1.570 ms. For most Eu^{3+}-doped oxides, the lifetimes in the literature are in the range of 1.4–2.0 ms, which are in the domain of the lifetimes for transparent ceramic film [38–40].

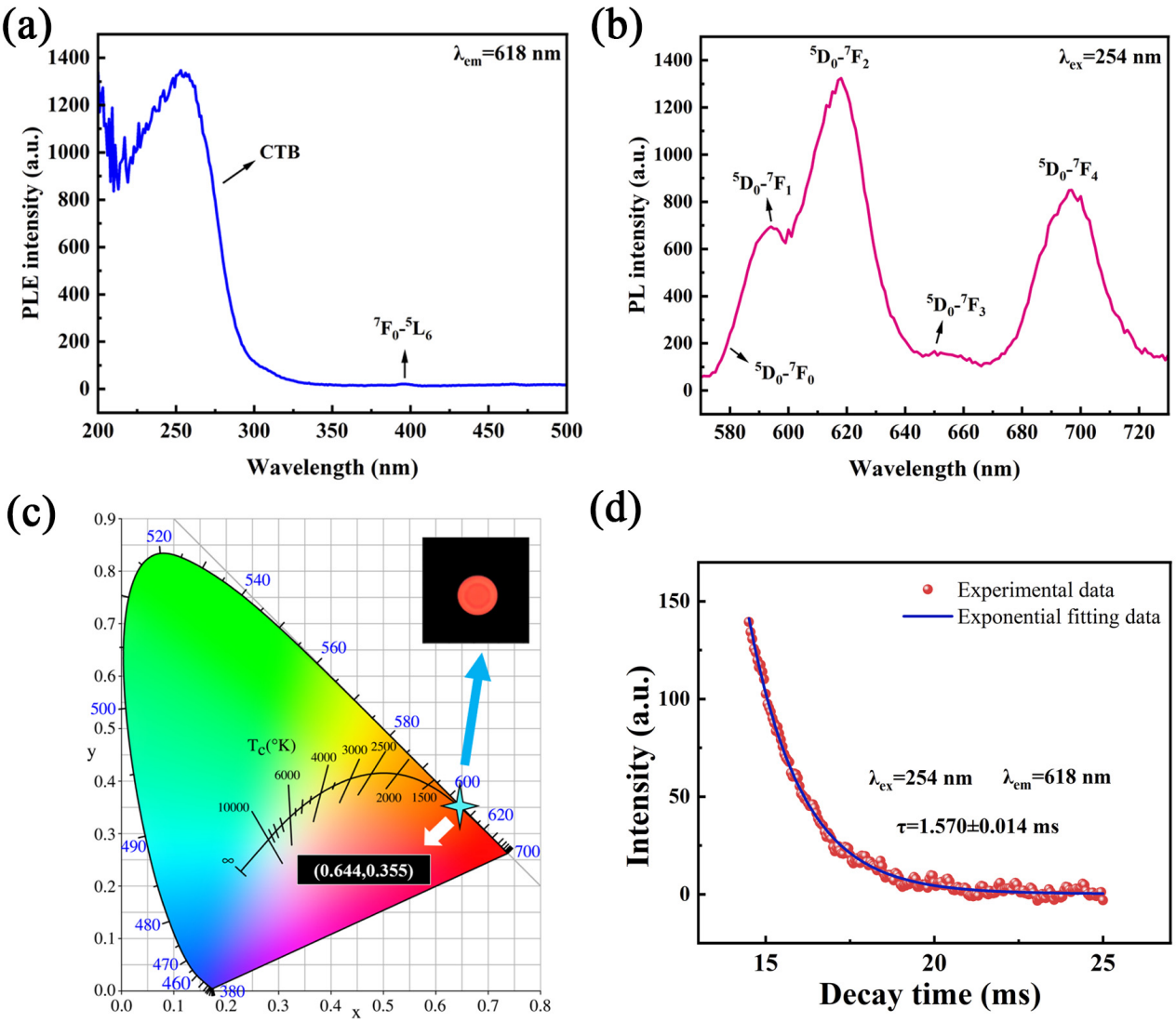

Figure 6. (**a**) PLE, (**b**) PL spectra, (**c**) CIE chromaticity diagram, and (**d**) fluorescence decay curve with fitting results of the ceramic film calcined at 1550 °C.

4. Conclusions

In this work, the two-dimensional guidance strategy has been successfully carried out for the perovskite-structured aluminate ceramic film. Through the interfacial reaction, $GdAlO_3:Eu^{3+}$ (GAP:Eu^{3+}) films of transparent ceramic were fabricated using the exfoliated layered gadolinium hydroxide nanosheets as the rare-earth source. The final films were tested by the characterization techniques, including XRD, SEM, TEM, FT-IR, PLE/PL spectroscopy, temperature-dependent PL spectroscopy, and luminescence decay analysis. The perovskite film of transparent ceramic can be obtained by calcining the LRH nanosheets on the substrate of amorphous alumina at 1550 °C in air for 120 min. Because the reaction takes place at the interface, the temperature-dependent element diffusion takes the dominant role and more reactants participate in the reaction with increasing calcination temperature. The grains for ceramic film increase up to 2–5 μm by elevating the temperature to 1550 °C, but the grains are much smaller than that for bulk ceramic. The lower temperature and interface diffusion contribute to the smaller grains. The ceramic film exhibits a high transmittance above 90% at the visible wavelength range. Upon UV excitation at 254 nm, the ceramic film emits intense red light with a lifetime of ~1.570 ms.

Supplementary Materials: The following supporting information can be downloaded at: https://www.mdpi.com/article/10.3390/coatings12121927/s1, Figure S1: EDS elemental mapping analysis of the film calcined at different temperatures; Figure S2: (a) Temperature-dependent PL spectra and (b) relative integral intensity of 618-nm emission bands.

Author Contributions: Conceptualization, methodology, T.Z. and Q.Z.; software, validation, formal analysis, investigation, resources, data curation, writing—original draft preparation, L.C. and J.Y.; writing—review and editing, visualization, T.Z.; supervision, project administration, funding acquisition, T.Z. and Q.Z. All authors have read and agreed to the published version of the manuscript.

Funding: This work was supported in part by the Natural Science Foundation of Liaoning Province (Grant 2020-MS-081), and National Natural Science Foundation of China (Grant 51302032 and U21A2045).

Institutional Review Board Statement: Not applicable.

Informed Consent Statement: Not applicable.

Data Availability Statement: This study did not report any public data.

Conflicts of Interest: The authors declare no conflict of interest.

References

1. Schubert, E.F.; Kim, J.K. Solid-state Light Sources Getting Smart. *Science* **2005**, *308*, 1274–1278. [CrossRef] [PubMed]
2. Zhou, Q.; Dolgov, L.; Srivastava, A.M.; Zhou, L.; Wang, Z.L.; Shi, J.X.; Dramicanin, M.D.; Brik, M.G.; Wu, M.M. Mn^{2+} and Mn^{4+} Red Phosphors: Synthesis, Luminescence and Applications in WLEDs. A Review. *J. Mater. Chem. C* **2018**, *6*, 2652–2671. [CrossRef]
3. Sun, B.H.; Zhang, L.; Zhou, T.Y.; Shao, C.; Zhang, L.; Ma, Y.L.; Yao, Q.; Jiang, Z.G.; Selim, F.A.; Chen, H. Protected-annealing Regulated Defects to Improve Optical Properties and Luminescence Performance of Ce:YAG Transparent Ceramics for White LEDs. *J. Mater. Chem. C* **2019**, *7*, 4057–4065. [CrossRef]
4. Yoon, S.W.; Park, H.K.; Ko, K.Y.; Ahn, J.; Do, Y.R. Various Nanofabrication Approaches towards Two-dimensional Photonic Crystals for Ceramic Plate Phosphor-capped WhiteF Light-emitting Diodes. *J. Mater. Chem. C* **2014**, *2*, 7513–7522. [CrossRef]
5. Park, H.K.; Yoon, S.W.; Choi, D.Y.; Do, Y.R. Fabrication of Wafer-scale TiO_2 Nanobowl Arrays via a Scooping Transfer of Polystyrene Nanospheres and Atomic Layer Deposition for Their Application in Photonic Crystals. *J. Mater. Chem. C* **2013**, *1*, 1732–1738. [CrossRef]
6. Zhu, Q.; Ding, S.N.; Xiahou, J.Q.; Li, S.Y.; Sun, X.D.; Li, J.G. A Groundbreaking Strategy for Fabricating YAG:Ce^{3+} Transparent Ceramic Films via Sintering of LRH Nanosheets on a Sapphire Substrate. *Chem. Commun.* **2020**, *56*, 12761–12764. [CrossRef]
7. Grabmaier, B.C. *Luminescent Materials*; Springer: Berlin, Germany, 1994; pp. 71–90.
8. Dorenbos, P.; Bougrine, E.; De Haas, J.T.M.; Van Eijk, C.W.E.; Korzhik, M.V. Scintillation Properties of $GdAlO_3$:Ce crystals. *Radiat. Eff. Defects Solids* **1995**, *135*, 321–323. [CrossRef]
9. Srivastava, A.M.; Brik, M.G. The Nature of Mn^{4+} Luminescence in the Orthorhombic Perovskite, $GdAlO_3$. *Opt. Mater.* **2017**, *63*, 207–212. [CrossRef]
10. Jovanić, B.R.; Andreeta, J.P. $GdAlO_3$:Cr^{3+} as a New Pressure Sensor. *Phys. Scr.* **1999**, *59*, 274–276. [CrossRef]
11. Wang, X.L.; Yang, Z.; Li, J.Y.; Fu, W.F.; Tang, P.; Chen, Y.F.; Guo, J.; Gao, Z.H.; Huang, Y.; Tao, Y. Hydrothermal Synthesis, Morphology and Luminescent Properties of $GdAlO_3$:Eu^{3+} Microcrystals. *J. Alloys Compd.* **2014**, *614*, 40–43. [CrossRef]
12. Shilpa, C.J.; Jayaram, A.K.; Dhananjaya, N.; Nagabhushana, H.; Prashantha, S.C.; Sunitha, D.V.; Sharma, S.C.; Shivakumara, C.; Nagabhushana, B.M. $GdAlO_3$:Eu^{3+}:Bi^{3+} Nanophosphor: Synthesis and Enhancement of Red Emission for WLEDs. *Spectrochim. Acta Part A Mol. Biomol. Spectrosc.* **2014**, *133*, 550–558. [CrossRef] [PubMed]
13. Jisha, P.K.; Naik, R.; Prashantha, S.C.; Nagabhushana, H.; Sharma, S.C.; Nagaswarupa, H.P.; Anantharaju, K.S.; Prasad, B.D.; Premkumar, H.B. Facile Combustion Synthesized Orthorhombic $GdAlO_3$:Eu^{3+} Nanophosphors: Structural and Photoluminescence Properties for WLEDs. *J. Lumin.* **2015**, *163*, 47–54. [CrossRef]
14. Michail, C.; Kalyvas, N.; Valais, I.; David, S.; Seferis, I.; Toutountzis, A.; Karabotsos, A.; Liaparinos, P.; Fountos, G.; Kandarakis, I. On the Response of $GdAlO_3$:Ce Powder Scintillators. *J. Lumin.* **2013**, *144*, 45–52. [CrossRef]
15. Kumar, P.; Singh, D.; Gupta, I.; Singh, S.; Kumar, V. Emerging green light emission of Er^{3+}-activated single phased $GdAlO_3$ phosphors for lighting applications. *Luminescence* **2022**, *ahead of print*.
16. Deng, T.L.; Jiang, X.B.; Zhang, Q.Y. Sustainably adjusting the up-conversion white-emitting luminescence properties of $GdAlO_3$:Er^{3+}/Yb^{3+}/Tm^{3+} phosphors. *Front. Chem.* **2020**, *8*, 788. [CrossRef]
17. Sheoran, S.; Singh, K.; Tanwar, V.; Singh, S.; Samantilleke, A.; Singh, D. Synthesis and Spectroscopic Investigations of Trivalent Europium-doped $Z_2Si_3O_8$ (Z = Mg, Ca and Sr) Nanophosphors for Display Applications. *Rare Metals* **2021**, *40*, 2610–2617. [CrossRef]
18. Xie, J.H.; Wang, J.; Qiu, G.H.; Li, X.B.; Huang, W.T.; Zhang, R.R.; Lin, T.; Wang, L.X.; Zhang, Q.T. A Strategy to Achieve Efficient Green-emission Dual-mode Luminescence of Yb^{3+}, Er^{3+} Doped $NaBiF_4$. *Rare Metals* **2021**, *40*, 2040–2048. [CrossRef]

19. Yao, J.; Zhu, Q.; Li, J.G. Garnet Transparent Ceramic Film of $Y_3Al_5O_{12}$:Eu^{3+} Fabricated through an Interface Reaction of Layered Rare-earth Hydroxide Nanosheets on Amorphous Alumina. *Appl. Surf. Sci.* **2022**, *579*, 152226. [CrossRef]
20. Zhu, Q.; Wang, X.J.; Li, J.G. Recent Progress in Layered Rare-earth Hydroxide (LRH) and its Application in Luminescence. *J. Adv. Ceram.* **2017**, *6*, 177–186. [CrossRef]
21. Zhu, Q.; Li, J.G.; Zhi, C.Y.; Li, X.D.; Sun, X.D.; Sakka, Y.; Golberg, D.; Bando, Y. Layered Rare-earth Hydroxides (LRHs) of $(Y_{1-x}Eu_x)_2(OH)_5NO_3{\cdot}nH_2O$ (x = 0–1): Structural Variations by Eu^{3+} Doping, Phase Conversion to Oxides, and the Correlation of Photoluminescence Behaviors. *Chem. Mater.* **2010**, *22*, 4204–4213. [CrossRef]
22. Li, J.G.; Sakka, Y. Recent Progress in Advanced Optical Materials Based on Gadolinium Aluminate Garnet ($Gd_3Al_5O_{12}$). *Sci. Technol. Adv. Mater.* **2015**, *16*, 014902. [CrossRef]
23. Hu, L.F.; Ma, R.Z.; Ozawa, T.C.; Sasaki, T. Exfoliation of layered europium hydroxide into unilamellar nanosheets. *Chem. Asian J.* **2010**, *5*, 248–251. [CrossRef] [PubMed]
24. Geng, F.X.; Xin, H.; Matsushita, Y.; Ma, R.Z.; Tanaka, M.; Izumi, F.; Iyi, N.; Sasaki, T. New layered rare-earth hydroxides with anion-exchange properties. *Chem. Eur. J.* **2008**, *14*, 9255–9260. [CrossRef] [PubMed]
25. Geng, F.X.; Matsushita, Y.; Ma, R.Z.; Xin, H.; Tanaka, M.; Iyi, N.; Sasaki, T. Synthesis and properties of well-crystallized layered rare-earth hydroxide nitrates from homogeneous precipitation. *Inorg. Chem.* **2009**, *48*, 6724–6730. [CrossRef] [PubMed]
26. Gadsden, J.A. *Infrared Spectra of Minerals and Related Inorganic Compounds*; Butterworth: Newton, MA, USA, 1975; pp. 101–120.
27. Nakamoto, K. *Infrared Spectra of Inorganic and Coordination Compounds*; John Wiley & Sons: New York, NY, USA, 1963; pp. 56–78.
28. Zhu, Q.; Li, S.Y.; Wang, Q.; Qi, Y.; Li, X.D.; Sun, X.D.; Li, J.G. Grafting of Terbium (III) Complexes onto Layered Rare-earth Hydroxide Nanosheets to Fabricate Novel Optical Fiber Temperature Sensors. *Nanoscale* **2019**, *11*, 2795–2804. [CrossRef] [PubMed]
29. Li, J.; Chen, F.; Liu, W.B.; Zhang, W.X.; Wang, L.; Ba, X.W.; Zhu, Y.J.; Pan, Y.B.; Guo, J.K. Co-precipitation Synthesis Route to Yttrium Aluminum Garnet (YAG) Transparent Ceramics. *J. Eur. Ceram. Soc.* **2012**, *32*, 2971–2979. [CrossRef]
30. Wen, L.; Sun, X.D.; Xiu, Z.M.; Chen, S.W.; Tsai, C.T. Synthesis of Nanocrystalline Yttria Powder and Fabrication of Transparent YAG Ceramics. *J. Eur. Ceram. Soc.* **2004**, *24*, 2681–2688. [CrossRef]
31. Zhu, Q.Q.; Li, S.X.; Yuan, Q.; Zhang, H.; Wang, L. Transparent YAG:Ce Ceramic with Designed Low Light Scattering for High-power Blue LED and LD Applications. *J. Eur. Ceram. Soc.* **2021**, *41*, 735–740. [CrossRef]
32. Zhu, Q.; Fan, Z.S.; Wang, S.; Xiahou, J.Q.; Li, J.G. Uniform Colloidal Spheres for RE_3BO_6 (RE = Eu-Yb, Y) and Excitation-dependent Luminescence of Y_3BO_6:Eu^{3+} Red Phosphor. *J. Am. Ceram. Soc.* **2019**, *102*, 7448–7461. [CrossRef]
33. Wang, Z.W.; Qu, Q.; Ji, H.P.; Hao, X.F.; Li, J.S. Available Manganese-containing Chemicals and Synthesis Methods for Mn^{4+}-activated Phosphors. *Chin. J. Lumin.* **2022**, *43*, 662–675. [CrossRef]
34. Zhu, Q.; Li, J.G.; Li, X.D.; Sun, X.D. Morphology-dependent Crystallization and Luminescence Behavior of (Y, Eu)$_2O_3$ Red Phosphors. *Acta Mater.* **2009**, *57*, 5975–5985. [CrossRef]
35. Syrbu, L.; Ursaki, V.V.; Tiginyanu, I.M.; Dolgaleva, K.; Boyd, R.W. Red and green nanocomposite phosphors prepared from porous GaAs templates. *J. Opt. A Pure Appl. Opt.* **2007**, *9*, 401–404. [CrossRef]
36. Sun, H.C.; Zhu, Q.; Li, J.G. Local Charge Regulation by Doping Li^+ in $BaGa_2O_4$:Bi^{3+} to Generate Multimode Luminescence for Advanced Optical Morse Code. *Ceram. Int.* **2022**, *48*, 9640–9650. [CrossRef]
37. Zhao, B.Q.; Zhu, Q.; Sun, X.D.; Li, J.G. Co-doping Zn^{2+}/Sn^{4+} in $ZnGa_2O_4$:Cr^{3+} for Dynamic Near-infrared Luminescence and Advanced Anti-counterfeiting. *Ceram. Int.* **2021**, *47*, 17000–17007. [CrossRef]
38. Mao, Q.; Shen, B.; Yang, T.; Zhong, J.S.; Wu, G.Q. A Double Perovskite-based Red-emitting Phosphor with Robust Thermal Stability for Warm WLEDs. *Ceram. Int.* **2020**, *46*, 19328–19334. [CrossRef]
39. Raju, G.S.R.; Jung, H.C.; Park, J.Y.; Moon, B.K.; Balakrishnaiah, R.; Jeong, J.H.; Kim, J.H. The Influence of Sintering Temperature on the Photoluminescence Properties of Oxyapatite Eu^{3+}:$Ca_2Gd_8Si_6O_{26}$ Nanophosphors. *Sens. Actuator B-Chem.* **2010**, *146*, 395–402. [CrossRef]
40. Bai, X.; Song, H.W.; Yu, L.X.; Yang, L.M.; Liu, Z.X.; Pan, G.H.; Lu, S.Z.; Ren, X.G.; Lei, Y.Q.; Fan, L.B. Luminescent Properties of Pure Cubic Phase Y_2O_3/Eu^{3+} Nanotubes/Nanowires Prepared by a Hydrothermal Method. *J. Phys. Chem. B* **2005**, *109*, 15236–15242. [CrossRef] [PubMed]